

LA-UR-21-22405

Approved for public release; distribution is unlimited.

Title: Multiscale Patterning from Competing Interactions and Length Scales

Author(s): Bishop, Alan

Intended for: past publication

Issued: 2021-03-10

Disclaimer:

Los Alamos National Laboratory, an affirmative action/equal opportunity employer, is operated by Triad National Security, LLC for the National Nuclear Security Administration of U.S. Department of Energy under contract 89233218CNA000001. By approving this article, the publisher recognizes that the U.S. Government retains nonexclusive, royalty-free license to publish or reproduce the published form of this contribution, or to allow others to do so, for U.S. Government purposes. Los Alamos National Laboratory requests that the publisher identify this article as work performed under the auspices of the U.S. Department of Energy. Los Alamos National Laboratory strongly supports academic freedom and a researcher's right to publish; as an institution, however, the Laboratory does not endorse the viewpoint of a publication or guarantee its technical correctness.

MULTISCALE PATTERNING FROM COMPETING INTERACTIONS AND LENGTH

SCALES

Dr. Alan Bishop

Los Alamos National Laboratory

email: arb@lanl.gov

Keywords

Competition, constraints, mesoscale, microstructure, elasticity

Abstract

We live in an era of complexity marked by impressive new tools powering the scientific method to accelerate discovery, prediction, and control of increasingly complex systems. In common with many disciplines and societal challenges and opportunities, materials and condensed matter sciences are beneficiaries. The volume and fidelity of experimental, computational, and visualization data available, and tools to rapidly interpret them, are remarkable. Conceptual frameworks, including multiscale, multiphysics modeling of this complexity, are fueled by the data and, in turn, guide directions for future experimental and computational strategies. In this spirit, we discuss the importance of competing interactions, length scales, and constraints as pervasive sources of spatio-temporal complexity. We use representative examples drawn from materials and condensed matter, including the important role of elasticity in some technologically important quantum materials.

1. INTRODUCTION

Over the last few decades there has been transformational change in the materials communities' ability to synthesize a great variety of hard, soft, and biological matter, to accurately measure its properties on multiple spatial and temporal scales, and to faithfully simulate and visualize significantly complex systems on physically relevant scales. Fig. 1 illustrates a (subjective) schematic of that history.

We are now reaping the benefits of this productive period and experiencing a golden age on the path to the holy grail of materials science—understanding and controlling synthesis–structure–property relationships, and using them to design materials with desired functionalities. On this journey toward more successful conceptual theoretical and modeling frameworks, it has been important to bring together traditional metallurgical and materials frameworks with solid state, condensed matter and many-body physics concepts and experimental/theoretical tools: e.g., appreciating the intrinsic roles of both structure and entropic fluctuations, ordered and disordered materials, the coupling of spin, charge, lattice and orbital degrees-of-freedom, and the roles of dimensionality, geometry and topology. This has led to an increase in the understanding of multiscale, multiphysics frameworks, and the essential functional roles that specific scales play in controlling materials behaviors and applications. In this article, we emphasize currently studied quantum materials such as pervoskites.

To place this era in a broader science and technology context, we note that it has appropriately been labelled the “century of complexity” (1, 2). Data are now available from

new generations of experimental probes and sensors—from biology to cosmology and from deep oceans to the deep space. The data are fortunately matched by equally notable advances in computational power and architectures, co-designed with algorithms to address significantly more realistic multiscale, multiphysics, and multi-functional phenomena. The massively greater volume and fidelity of the experimental and simulation data are resulting in powerful partnerships of data science with application and discipline specific expertise to extract relevant patterns, even in situ and on-the-fly, to inform more predictive theory and simulations and guide experiments. The nature of the phenomena now being tackled are in many cases “complex systems and networks,” requiring not only the new tools but new concepts, where reductionism is extended beyond isolating individual functions from their environment to identifying key collective elements which couple strongly into a system.

A fundamental issue for such complex systems is understanding, measuring, simulating, modeling, controlling, and applying “mesoscale” collective spatial patterns and their dynamics. The mesoscale elements are often the critical and rate-limiting bridges between microscopic and macroscopic levels of description for relevant macroscopic functions — faithfully passing information between these scales lies at the heart of all predictive multiscale descriptions. While this mesoscale importance applies to many disciplines, the discussion here is limited to a sampling of examples from materials and condensed matter. The complexity origins discussed are not exhaustive but intended to illustrate some important origins of mesoscopic patterns in materials, including the importance of elasticity in many currently studied quantum materials.

Patterns are typically the result of competitions of scales. In turn, these competitions are frequently the result of coupled degrees-of-freedom, which produce effective nonlinearities and hence intrinsic new scales. In materials and condensed matter, the degrees-of-freedom include spin, charge, orbital, and lattice, as well as their coupling to external fields (stress, electrical, magnetic, optical, etc.) Early examples of this perspective can be found in Ref. (3).

Lattice dislocations (and more generally discommensurations) are familiar mesoscopic (topological) textures in materials, controlling important macroscopic properties such as slip, yield, and transport. Edge and spiral dislocations also appear in multi-dislocation patterns. Together with their relatives, twins and tweed, these mesoscale structures are essentially the result of competing energies — potential, strain, kinetic — and constraints. This feature of competitions and constraints is the focus of the examples below.

2. STRAIN-BASED ELASTICITY: THE ROLE OF CONSTRAINTS

Even one-dimensional (1-d) lattices with competing interactions can exhibit emergence of incommensurate mesoscopic patterns as ground states and excitations. Ref. (4) is an early example, extending the familiar Frenkel-Kontorova model of dislocations with non-convex interparticle (strain) interactions. This results in twinning-like patterns and was a precursor to later atomic-scale formulations of elasticity in general-d, introducing essential lattice symmetry and compatibility constraints, which we now discuss.

Symmetry-constrained coupling of acoustic and optic modes is key to strong on-lattice (off-lattice is a different analysis path) elasticity, resulting in intrinsic multiscale phenomena — atomic-scale distortions affect structural patterns at long ranges and boundaries, and vice versa. This is especially important in electronically localized (d, f-shell) quantum materials, including perovskites. The localized orbitals lead to many novel localization–delocalization charge/orbital/spin broken-symmetries, but ALSO strong, long-range and anisotropic elasticity.

For illustration, we consider here the class of materials known as ferroelastic martensites. Ferroelasticity is the existence of two or more stable orientation states of a crystal that correspond to different arrangements of the atoms, but are structurally identical (enantiomorphous) (5). These orientation states are degenerate in energy in the absence of mechanical stress. The term martensitic usually refers to a diffusionless first-order phase transition that can be described in terms of one (or successive) shear deformations from a parent to a product phase. [Schematic illustrations in two-dimensional (2-d) cases are shown in Fig. 2.] The morphology and kinetics of the transition are dominated by the strain energy, and the transition results in characteristic lamellar (twinned) microstructures.

Features observed in proper ferroelastic crystals include mechanical hysteresis and mechanically switchable domain patterns. Ferroelasticity usually occurs as a result of a phase transition from a nonferroelastic high-symmetry parent phase and is associated with the softening of an elastic modulus with decreasing temperature or increasing pressure in the parent phase. Since the ferroelastic transition is normally weakly first order, or second

order, it can be described to a good approximation by Landau theory with spontaneous strain or deviation of a given ferroelastic orientation state from the parent phase as the order parameter (OP). The strain can be coupled to other fields such as electric polarization and magnetic moment, and thus the crystal can have more than one transition.

Dynamics plays a central role in proper ferroelastic transitions (5, 6, 7). These materials undergo diffusionless, displacive transitions, with strain components as the primary OP, and develop complex microstructures during their evolution, finally forming spatially varying, multiscale textures (strain patterns). Ferroelastics include materials of technological importance such as superconducting cuprates (8) and colossal magnetoresistance manganites (9).

Many dynamical models have been proposed (see Ref. 6) to follow specific aspects of ferroelastic pattern formation such as nucleated twin-front propagation, width length scaling of twin dimensions, tweed, stress effects, elastic domain misfits, acoustic noise generation, etc. In Ref. (6), symmetry-specific OP strain dynamics are derived for proper ferroelastics, determining the precise form of long-range potentials that emerge, as well as the regime of validity of time-dependent Ginzburg Landau (TDGL) equations for strain dynamics, including explicit noise terms. A central role is played by the N_c “St. Venant compatibility conditions” (10) for the $N=N_{op}+n$ symmetry adapted strains, which encode the absence of broken bonds (i.e., ensure lattice integrity), and allow the n non-OP strains to be expressed in terms of N_{op} order parameter strains. (Lattice defects and ruptures are an extension of this approach.) The following is shown in (6): (i) An underdamped set of

N_{op} equations can be obtained for the OP strains alone with naturally emerging anisotropic, long-range contributions to OP potentials, friction, and noise; (ii) The same OP equations can be obtained either by varying the displacement or by varying the strains subject to the compatibility constraint through dynamic Lagrange multipliers; and (iii) Omitting strain inertial terms yields strain TDGL equations with (in general) nonlocal Onsager coefficients controlling late-time dynamics for the damping envelope of texture oscillations.

Explicit numerical demonstrations of (i), (ii), (iii) for the 2-d triangular to centered rectangular or TR lattice transition ($N_{op}=2, n=1, N_c=1$) and for the square to rectangular or SR lattice transition ($N_{op}=2, n=2, N_c=1$), as well as dynamics for all other allowed 2-d symmetries are detailed in (6). The procedure can be generalized to 3-d, e.g., cubic to tetragonal ($N_{op}=2, n=4, N_c=6$) (11).

The central result is dynamics written in the OP strains $\{\varepsilon_i\}$ $\ell = 1, 2 \dots N_{op}$ alone,

$$\rho_0 \ddot{\varepsilon}_\ell = \frac{c_\ell^2}{4} \vec{\Delta}^2 \left(\frac{\delta(F+F^c)}{\delta \varepsilon_\ell} + \frac{\delta(R+R^c)}{\delta \dot{\varepsilon}_\ell} \right) + \tilde{g}_\ell + \tilde{g}_\ell^c, \quad \text{Eq. 1}$$

where c_ℓ is a symmetry-specific constant, and ρ_0 is a scaled mass density. $F^c(\{\varepsilon_\ell\}), R^c(\{\dot{\varepsilon}_\ell\})$ are the compatibility-induced symmetry-specific contributions that emerge explicitly from the non-OP free energy as additions to the OP free energy F and OP Rayleigh dissipation R , while \tilde{g}_ℓ^c is the corresponding noise term that adds to the OP noise \tilde{g}_ℓ . In Eq. (1), the symbol $\vec{\Delta}$ is used to denote dimensionless discrete derivatives on a reference lattice. The

equations can be written (6) as Langevin equation for $\varepsilon_i(\vec{k}, t)$ and $v_i = \dot{\varepsilon}_i(\vec{k}, t)$, yielding statistically equivalent Fokker-Planck equations for the probability $P(\{\varepsilon_i, v_i\}, t)$.

The N_{op} strain order-parameter equations with derived explicit anisotropic long-range terms are equivalent to the d displacement equations that do not explicitly have such terms. An advantage of the OP strain approach is that it uses those anisotropic long-range correlations, which are valuable in understanding simulated textures and relating to other systems with long-range interactions (see below). The compatibility conditions can be viewed as the integrability conditions for the strain tensor as a function of the displacement field. The compatibility equation for strain has also been used for a consistent description of forces in liquids; (12, 6). This approach is in the spirit of the Landau description of phase transitions: (13) namely working with the order parameters as the basic physically relevant variables, and focusing on the order-parameter symmetries (as encoded in the lattice compatibility factors), as the consequent source of ferroelastic texturing.

Full details of the symmetry-restricted GL analysis and dynamics can be found in (6). Here we illustrate in Figs. 3 and 4 some of the physical consequences of the combined effects of lattice-scale symmetry (compatibility) conditions and the long-range, anisotropic strains which they self-consistently induce. An extensive survey of this strain-based compatibility approach, with extensions to other 2-d and 3-d situations, can be found in (14).

3. COUPLING STRUCTURE WITH ELECTRONIC AND MAGNETIC FIELDS

In the spirit of this article, we now consider the effects of the above intrinsic elastic patterning on coupled electronic and magnetic degrees-of-freedom, which can inherit complementary multiscale spatio-temporal phenomena.

Electronic properties of twinned structures are discussed in (15). Here we consider, as another example, the intrinsic coexistence of distinct metallic and insulating electronic phases in a perovskite manganite (16, 17), such as $\text{La}_{1-x-y}\text{Pr}_y\text{Ca}_x\text{MnO}_3$, which presents opportunities for sensitively tuning the electronic properties. In particular, colossal magnetoresistance (18) in these materials is closely related to the observed texture owing to coexisting nanometer- and micrometer-scale inhomogeneities. Extensive data from various high-resolution probes show the existence of such inhomogeneities (16, 17). Experimental results also support the presence of metastable states in manganites. For example (see Ref. 16, 17), magnetic fields or X-rays have been used to convert insulating regions into ferromagnetic metallic ones, which are stable even when the fields are removed. Explanations based on electronic mechanisms and chemical disorder (16, 17) have not been sufficient to describe the multiscale, multiphase coexistence within a unified picture. Lattice distortions and long-range strains are known to be important in the manganites (19). In Ref. (16), it is shown that the texturing can be due to the intrinsic complexity of a system with strong coupling between the electronic and elastic degrees of freedom. This leads to “landscapes” of energetically favorable configurations and provides a natural mechanism for self-organized inhomogeneities.

To capture salient aspects of electron–lattice coupling in manganites, Ref. (16) uses a model in which the phase with short-and long-wavelength lattice distortions is insulating, and that without lattice distortion is metallic. The structural templates then drive novel electronic, magnetic, and optical properties. This approach also provides a basis for understanding other observed features (see Ref. 16, 17), such as precursor short-range ordering and quasi-elastic scattering near the phase-transition, hysteretic and glassy dynamics, metastability and photo-induced insulator–metal transitions.

The lattice distortions in manganites closely follow the state of the outermost shell (e_g) electrons on Mn ions through a Jahn–Teller coupling (19). If an e_g electron is localized at a Mn site in the insulating phase, the symmetry of the surrounding oxygen octahedron is lowered from cubic to tetragonal. At low temperatures, the distorted octahedra stack in specific patterns, referred to as charge and orbital ordering. For example, in $\text{La}_{0.5}\text{Ca}_{0.5}\text{MnO}_3$, the long Mn–O bonds of the elongated octahedra form a zigzag pattern in the x–y plane (20), giving rise to short-wavelength lattice distortions. The stacking of the short Mn–O bonds along the z-direction is responsible for the long-wavelength tetragonal (more accurately orthorhombic) distortion. Such lattice distortions are absent in the metallic phase because the e_g electrons are delocalized.

Coupled short- and long-wavelength modes in a cubic anharmonic elastic energy (see Fig. 5 caption) give rise naturally to an energy landscape with multiple energy minima. For illustration, we consider here two cases with different harmonic moduli for short-wavelength lattice distortions as shown in Fig. 5, one giving a shallow (blue curve, a small

modulus) and the other a deep (red curve, a large modulus) local minimum for the undistorted phase. Solid circles in the inset represent locations of energy minima for our model. The modulus can be changed, for example, by varying the average size of the rare-earth and alkali-metal ions (often as parametrized as a “tolerance factor”) (21).

Figure 6a–h shows the sequential relaxations for the shallow local minimum case starting from random initial s_x and s_y values (see Fig. 5 caption), corresponding to a rapid quenching of the system from high temperature. The results are conveniently represented in terms of $p_3 = s_x^2 - s_y^2$. Positive (red) and negative (blue) values of p_3 correspond to different orientations of short- or long-wavelength lattice distortions (s_x with negative e_3 and s_y with positive e_3). The short- and long-wavelength mode distortions are simultaneously generated through the minimal symmetry-allowed coupling between e_3 and s_x^2, s_y^2 at each site. The green regions with zero p_3 have no distortions. Most of the region initially relaxes to the undistorted local minimum state (Figs. 6c and d), because the rapidly fluctuating initial field contains few components of the long-wavelength strain modes, making it difficult for the system to reach the global minimum. However, even in the presence of the random field, there are regions with some correlation, which eventually lead to nanometer-scale nucleating droplets. Comparison of Fig. 6b–d shows that there is a critical strength and size of these droplets, a common feature of first-order phase transitions. However, here the long-range nature and anisotropy of the interaction between strain fields control the nucleation process (16), and are a likely source of the observed nanometer-scale inhomogeneities (16, 17), the anisotropic short-range precursor

correlations at high temperatures, and the quasielastic central peak in neutron scattering near the metal–insulator phase-transition.

Figures 6i and j shows the calculated tight-binding electronic structure supported by the lattice distortion template in Fig. 6f. For illustration, we have used a Su–Shrieffer–Heeger (SSH) electron–lattice coupling model (22) (with one electron per site) to incorporate the dependence of the electron transfer probability on interatomic distances. This SSH model, together with the specific coupling between short- and long-wavelength lattice modes, gives rise to electronic phases for undistorted and distorted structures. The typical local electronic density of states (DOS) versus electronic energy shown in Fig. 6j indeed indicates a metallic local DOS in the undistorted region and a gapped (insulating) local DOS within the distorted region. For the Fermi energy $E_f = 0$, the local DOS configuration in direct space is shown in Fig. 6i. This illustrates the coexistence of metal (green) and insulator (blue) associated with the elastic texture template, similar to that observed in manganites (23). For the deeper local-minimum case, the simulation of the annealing process from random initial configurations shows characteristic features of metastability or a supercooled state, such as a low probability of creating nucleation droplets. A typical result is shown in Fig. 7a. The energy landscape near the undistorted state is deep enough that the coexisting phase of metal and insulator is stable, unlike the shallow local-minimum case above. Such stable coexistence of metallic and insulating domains is similar to the submicrometer size multiphase coexistence observed in, e.g., $\text{La}_{1-x-y}\text{Pr}_y\text{Ca}_x\text{MnO}_3$ (24). Thermal fluctuations at finite temperatures can slowly grow the distorted region — such slow, history-dependent dynamics with time-scales that range from minutes to hours has

also been observed in various manganites (25). Figures 7b, c show the corresponding electronic inhomogeneities within our SSH model. The local DOS for the sites deep within the domain shows a clear gap near electronic energy $E = 0$. Thus, for $E_f = 0$, the metallic and insulating phases coexist with relatively sharp boundaries, as observed in STM images (23). A magnetic field is expected to modify the energy landscape in favor of the undistorted ferromagnetic metallic state, consistent with reduction of the quasi-elastic scattering spectral weight by applied magnetic fields (26).

The above results illustrate how the micrometer-scale multiphase coexistence can be self-organized and result from the presence of an intrinsic elastic energy landscape. Because the domain formation is self-sustained, external stimuli such as optical lasers, X-rays, or ultrasonic standing waves can be used to sensitively manipulate patterns of metallic and insulating regions, thus making the control of nano-engineered functional structures feasible (15, 27).

The mechanisms we have proposed here can be applied to describe intrinsic inhomogeneities in other materials with strong bonding constraints, such as relaxor ferroelectrics and high-transition-temperature (high- T_c) superconducting oxides, where the functionalities may also be mediated through self-organized lattice distortions (28). More generally, there are many materials where the above approach to coupling lattice, spin, charge, and orbital degrees-of-freedom, including elastically-driven transitions, can be applied. For instance, epitaxial oxide layers and multilayers provide extensive tunability for technology (29), and magnetocalorics (30) are studied for their potential application as

efficient refrigeration and waste-recovery materials. There, as in many realistic applications, the above analysis applies to individual grains, with the intra-grain textures providing stresses for inter-grain interaction and growth. Multi-grain structures are beyond the scope of the present discussion but usually require coarser-scale (e.g., phase-field and finite-element) modeling.

5. ELASTICITY-DRIVEN SELF-ORGANIZATIONS OF SMALL POLARONS

Although the situation is improving with computing power, *ab initio* supercell calculations for localized orbital (d, f) materials are not well-suited to capturing mesoscopic landscapes, including elasticity effects. Of course, elasticity has its origins in the total energy of a solid, including the Coulomb contributions. Indeed, if atoms are allowed to relax self-consistently in a Coulomb field, many of the elasticity features above (multipole screening, etc.) must be recovered. We will illustrate similar long-range field effects in examples below. However, first we consider, (31), as a second example of coupling strain with other degree-of-freedom, elasticity-driven self-organization of small polarons. In Ref. (3), it is shown that, in a generalization of the adiabatic Holstein polaron model (31), a bound polaronic state acts as an impurity and induces strong long-range, angular dependence in long-range elastic fields but a localized electronic core. The elastic fields thus provide an anisotropic, indirect interaction between polarons extending to large distances. For a given density of polarons, this interaction favors the formation of strings of polarons in preferred directions. Ref. (31) demonstrates this on a 2-d square lattice.

The symmetry-adapted, principal strains for a 2-d square lattice can be written as

$$e_1 = \frac{1}{\sqrt{2}}(\epsilon_{xx} + \epsilon_{yy}); \quad e_2 = \frac{1}{\sqrt{2}}(\epsilon_{xx} - \epsilon_{yy}); \quad e_3 = \epsilon_{xy} = \epsilon_{yx} ,$$

where e_1 is the compressional or dilatational strain, e_2 the deviatoric strain, and e_3 the shear strain associated with a unit cell. In the small strain regime, the Lagrangian strains, ϵ_{ij} , are defined by

$$\epsilon_{ij} = \frac{1}{2} \left(\frac{\partial u_i}{\partial x_j} + \frac{\partial u_j}{\partial x_i} \right) ,$$

where u_i , $i=1,2$ are the two displacements in the x and y directions. As noted in Section 2, the three strains in 2-d are not all independent and are related in a bond-intact medium by the St. Venant compatibility (6) constraint

$$\partial_x^2 \epsilon_{yy} + \partial_y^2 \epsilon_{xx} - 2\partial_x \partial_y \epsilon_{xy} = 0 ,$$

which in terms of the symmetry adapted strains becomes

$$(\partial_x^2 + \partial_y^2)e_1 - (\partial_x^2 - \partial_y^2)e_2 - \sqrt{8}\partial_x \partial_y e_3 = 0 .$$

The displacements can be obtained as derived variables, within an arbitrary constant, from strain by Fourier transformation.

In (31), a quantum particle (charge) is introduced as an extension of the Holstein polaron model. The elastic distortions of the lattice and the particle's quantum wave-function are then deduced self-consistently in an adiabatic approximation. Here, we illustrate the results for multiple polarons in Fig. 8. For strong charge-lattice coupling, the polarons are electronically very localized (small polarons), but their effect on the strain fields is long-ranged and highly directional, reflecting the discrete square lattice symmetry. Notice the effect of the strain on the polaron ordering into filamentary landscapes of strings. Natural extensions include effects of disorder, chemical structure, interfaces, and microstructure on polaron patterns.

Small polaron center of mass motion (quantum tunneling) is very slow due to Peierls-Nabarro lattice pinning. However, an interesting addition to the above effects of elasticity on polarons is to include the internal quantum mechanical tunneling dynamics of coupled charge and lattice (bond-lengths) within a polaron. This intrinsic local dynamics results in a dynamical screening of the long-range elastic fields (32), depending on the tunneling frequency. Since the internal tunneling rate is slow for small polarons, the screening is weak but it becomes stronger (i.e., reduces the elastic range) as the tunneling rate increases with polaron size. Simultaneously, the polaron mass increases and the lattice barrier to polaron center-of-mass translation decreases.

5. COEXISTING SHORT- AND LONG-RANGED INTERACTIONS

The above examples of elastically-driven multiscale textures are examples of a much larger class of phenomena resulting from coexisting short- and long-range interactions. Ref. (33) describes many cases. Here we use a few examples to emphasize some important features.

Josephson Junction Arrays (JJAs) are a fascinating template on which to study connections between space and time in complex dynamical systems. Many experimental and simulation studies have been made for 1-d, 2-d and 3-d JJAs (see Ref. 34), revealing the importance of magnetic flux patterns (induced by applied magnetic fields) and their dynamics.

As an example, we summarize here molecular dynamics (MD) simulations of one specific 2-d case (34) to demonstrate the phenomena of “glassy” dynamics observed in many materials and condensed matter systems (3, 35). Extensions to 3-d JJAs studied with Langevin MD can be found in Ref. (36). We consider the relaxation from an initially random flux state and follow the multiple length and time scales involved. This noisy relaxation is controlled by the dynamics of various “defect” structures (specifically topological vortices and domain walls) defined with respect to the underlying ground-state flux structure. As in traditional materials science (3), the mesoscopic defects, their collective patterns, and their dynamics control a complex macroscopic response, but are themselves microscopically controlled by the competitions producing the ground-state flux complexity. The case we show is controlled by competition between symmetries — the square symmetry of an underlying lattice and the preferred hexagonal (Abrikosov) symmetry of flux patterns induced by an applied magnetic field. Multiscale responses have been observed in many other competing interaction systems (3, 35, 37). Various “creep” and “stretched-

exponential” regimes have been proposed (38), as well as phenomenological scaling theories relating spatial domain sizes with temporal scales (39).

The Hamiltonian for the JJA takes the form (34)

$$\mathcal{H} = -E_0 \sum_{i,j} [\cos(\theta_{ij} - \theta_{i-1j} - A_{i-1j,ij}) + \cos(\theta_{ij} - \theta_{ij-1} - A_{ij-1,ij})], \quad \text{Eq. 2}$$

where θ_{ij} is the phase of the superconducting island with the discrete coordinates (i,j) of the lattice, and $A_{ij,kl} \equiv (2e/\hbar c) \int_{ij}^{kl} \mathbf{A} \cdot d\mathbf{l}$ is the integral of the vector potential from island (i,j) to a neighboring island (k,l) . The critical current of a junction is given by $I_0 \equiv (2e/\hbar)E_0$ and the applied current enforced by boundary conditions is $I_1 = (2e/\hbar)E_1$. The $A_{ij,kl}$ summed around a square plaquette obeys:

$$A_{ij,i-1j} + A_{i-1j,i-1j-1} + A_{i-1j-1,ij-1} + A_{ij-1,ij} = 2\pi f ,$$

where the “frustration” $f = Ha^2/\Phi_0$ is a constant giving the average number of flux quanta $\Phi_0 = hc/2e$ of the external magnetic field H through the area a^2 of each plaquette of the array. We also introduce the fractional charge q_{ij} , obtained as the gauge-invariant phase sum around the ij th plaquette:

$$q_{ij} = (1/2\pi)[(\theta_{ij} - \theta_{ij-1} - A_{ij-1,ij})\text{mod}\pi + (\theta_{ij-1} - \theta_{i-1j-1} - A_{i-1j-1,ij-1})\text{mod}\pi \\ + (\theta_{i-1j-1} - \theta_{i-1j} - A_{i-1j,i-1j-1})\text{mod}\pi + (\theta_{i-1j} - \theta_{ij} - A_{ij,i-1j})\text{mod}\pi] .$$

Eq. 3

We limit discussion here to the “maximal frustration” situation with $f = \frac{1}{2}$ uniformly. Then $q_{ij} = \pm \frac{1}{2}$: the ground state is a checkerboard pattern and thus it is convenient to introduce the staggered order parameter $\bar{q}_{ij} = (-1)^{(i+j)}q_{ij}$. In (34), quenching to a prescribed equilibrium temperature of an initially random flux configuration was performed, with dynamics introduced, including thermal noise, in a classical Langevin MD form. The following global and gauge-invariant quantity $C(t)$ was monitored in time:

$$C(t) = N^{-2} \sum_{i,j} q_{ij} (q_{i+1j} + q_{i-1j} + q_{ij+1} + q_{ij-1}) .$$

Fig. 9 shows the global quantity $C(t)$ for various temperatures T . It is important to note that the transition temperature T_c for $f = \frac{1}{2}$ is $T_c = 0.45$ (34); for $T > T_c$ long-range flux order and superconductivity are lost. T_c takes the form of a Kosterlitz–Thouless topological phase transition for $f = \frac{1}{2}$, where vortex-antivortex unbinding begins. For other values of f , two distinct transitions occur: vortex-driven and domain-wall-driven order-disorder. Effects of disorder are also considered in Refs. 34 and 40.

$C(t)$ is displayed for a selection of temperatures in Fig. 9 to illustrate the following time observed dependences:

i. $T \ll T_c$ and short times. Here, flux creep is observed with $C(t) \sim \ln(t)$ [Fig. 9(a)]. The asymptotic value of C first decreases as T is increased from $T \ll T_c$ and then increases again ($T \gtrsim T_c$). This can be understood as trapping into a metastable flux configuration at very low T because of the uniform frustration; as T is increased, thermal tunneling over the frustration barriers is allowed and C approaches closer to its ground state value (-1); at higher T (\geq frustration pinning energy) thermal randomization occurs ($C \rightarrow 0$ for $T \gg T_c$). This interpretation is supported by the time evolutions of the actual flux structures (See Ref. 34). At low T , a \bar{q}_{ij} structure is observed which is frozen after its initial relaxation but continues to slowly evolve at intermediate T and is nearly random at high T .

ii. **Intermediate T ($0.3T_c \lesssim T \lesssim 0.7T_c$)** Here, after the initial rapid relaxation, we observe [Fig. 9(b)] an excellent fit to a glassy (stretched-exponential) form of relaxation (39). Specifically, Fig. 9(b) shows the fit to $C_t \sim \exp[-(t/\tau)^\beta]$, for which we find $\beta = 0.45$ ($T = 0.2$). Strikingly, essentially the same β value is found (34) for the whole temperature range, suggesting a common mechanism. Indeed, studies of flux structure evolution (34) identifies the detailed domain growth mechanisms controlling this slow relaxation regime — namely, interrelated roles of domain wall and vortex defects with respect to the $f = \frac{1}{2}$ flux ground state, with domains growing by vortex–antivortex pairs nucleating, attaching to domain walls, and then counter propagating around the domain.

iii. **$T \sim T_c(0.45)$.** Here critical effects dominate. A behavior of the form $C_t \sim \exp[-[\ln(t/\tau)]^\delta]$ is in fair agreement [Fig. 9(c)] for $T \sim T_c$, with $\delta \sim 0.9$. For $T > T_c$ the flux lattice melts.

It is interesting to understand the connections between many time scales and many length scales in glassy systems. Phenomenological theories based on typical clusters have been proposed, e.g., the Lifshitz-Slyozov (39) law. In Ref. (34), the spatial Fourier transform $g(k)$ was monitored. This function is sensitive to the distribution of domain sizes rather than the detailed structure of domain walls. The disordered phase at $T > T_c$ is indeed characterized (34) by weight on many k scales, whereas the large domain structures for $T = 0.25$ are characterized by only a few dominant k scales.

As another illustrative example of coexisting short- and long-range interactions, we now discuss the thermal fluctuations of particles in a 2-d computational box that have a short-range dipolar attraction and a long-range repulsion (41).

Mesoscopic and inhomogeneous ordering of charges in diverse materials such as (41) high- T_c superconductors, colossal magnetoresistant manganites, and 2-d electron gas systems has been a subject of intense study, for properties including superconductivity, pseudogaps, and transport and magnetic responses. The phases include labyrinths, stripes, and clusters, and often consist of “soft” intermediately ordered patterns, lying between completely ordered and completely disordered systems (42, 43). For example, inhomogeneous charge-ordering phases can be produced by a competition between repulsive and attractive interactions. In the case of the metal oxides, holes with a repulsive Coulomb interaction reside in, e.g., an antiferromagnetic background, with the distortion of the spins giving rise to a dipolar attraction between holes, and allowing the formation of clump, Wigner crystal, and stripe phases (44). A variety of other microscopic mechanisms

produce a similar coexistence of long-range repulsion competing with directional short-range attraction in a wide range of systems, such as defects or dislocations in elastic media, covalent glasses, systems with a finite density of small polarons (above), and soft matter (45).

For illustration, we focus here on the examples of a quasiclassical model (41) for charge ordering of holes in transition metal oxides, in which the particles have a Coulomb repulsion and a dipolar attraction. As a function of hole density (doping), we find an extended soft phase comprised of partially ordered filaments. Ordered clumps form for densities below this region, and ordered stripes (Wigner crystal-like phases) occur above it. The soft filamentary structures persist to high temperatures. Within the soft phase region there is a low temperature onset of motion along the filaments: the filaments act as a template for correlated percolation of particle motion. When the particle positions are averaged over long times, the filaments form a checkerboard pattern. All of the rich multiscale patterning and dynamics arises from a deceptively simple 2-d model (41) in which effective interaction between two holes, 1 and 2, a distance \mathbf{r} apart is given by

$$V(\tilde{\mathbf{r}}) = \frac{q^2}{\tilde{r}} - Ae^{-\tilde{r}/a} - B \cos(2\theta - \phi_1 - \phi_2) e^{-\tilde{r}/\xi} . \quad \text{Eq. 4}$$

Here $q = 1$ is the hole charge, θ is the angle between \mathbf{r} and a fixed axis, and $\phi_{1,2}$ are the angles of the magnetic dipoles relative to the same fixed axis. A is the strength of the short-range anisotropic interaction and B is that of the magnetic dipolar interaction

$[B \approx A/(2\pi\xi^2)]$, which we assume to be independent variables. Here we take $A = 0$ and assume $\xi \sim 1/\sqrt{n}$.

The static hole configurations, obtained with Monte Carlo simulations, are illustrated in Fig. 10. At low densities, cross-like clumps form and organize into an ordered lattice structure [Fig. 10(a)]. Above a density $n = 0.9$, the clumps begin to touch and are replaced by partially disordered filamentary patterns of the type illustrated in Fig. 10(b) for $n = 1.2$ and Fig. 10(c) for $n = 2.1$. These filamentary patterns persist within a glassy (soft) phase window that extends up to $n = 2.4$, where a more ordered anisotropic Wigner crystal pattern forms [Fig. 10(d)]. The transition from the filamentary pattern phase of Figs. 10(b) and 11(c) to the anisotropic Wigner crystal phase of Fig. 10(d) occurs when the interactions between the holes are dominated by the Coulomb repulsion.

For the clump region in Fig. 10(a), the superlattice clump structure remains stable up to a very high temperature: the superlattice and clumps break up simultaneously around $T_m = 930K$, where the melting temperature T_m is measured by the onset of diffusion (see Fig. 11 inset). In general, particles are confined within the clump up to this temperature. Such limited motion of particles within the clumps begins at around 700 K. The anisotropic Wigner crystal phases found at densities $n > 2.4$ beyond the filamentary soft phase are stable up to about 700 K. Above this temperature the entire pattern rapidly melts.

The fluctuations within the soft phase are interesting. Well below T_m , we find (41) a modulated liquid-like phase, in which the charges are constrained to remain within a

filamentary square pattern, but are free to move along the filaments. The filamentary square pattern observed throughout the soft phase contrasts with the clump phase where the holes remain localized within each clump. The modulated liquid phase remains stable up to the temperature T_m at which the pattern itself is destroyed. We can identify a second, lower melting temperature T_s at which the onset of the square (checkerboard) modulated liquid phase occurs. In this phase, the particle motion is constrained to follow the square template. Although the hole density is not high enough to create this structure as a static configuration, when the holes are moving their effective density increases, allowing them to form the square pattern.

The temperature T_s at which the square modulated liquid appears varies with doping. More disordered hole configurations have a lower T_s . The onset of the modulation occurs when the structure of the pattern begins to change globally due to local rearrangements of the holes. We can detect changes in the structure of the pattern by, e.g., monitoring the local orientation of a Voronoi polygon centered on each particle at fixed T (41). Changes in the pattern produce increased fluctuations of the local orientation. The onset of the modulated liquid occurs when enough particles are fluctuating on average to allow the excitations to percolate through the system. There is a clear decrease of T_s in the soft phase when the modulated liquid appears. T_s is shown as a function of density in Fig. 11, with a dramatic decrease in T_s throughout a soft phase window from $n \sim 0.9$ to $n \sim 2.4$. This corresponds to the geometrically disordered percolation phase. Outside of this soft window, particle motion does not occur until significantly higher temperatures are reached, especially for $n < 0.9$. In the soft phase window, we observe correlated percolation: the onset of

structural percolation coincides with a highly directional softness. This is in contrast to the isotropic melting that occurs at much higher temperatures. Thus, we have a system which contains a rigid template of soft filaments. At T_s , a type of dislocation mobility transition occurs in which a local excitation becomes delocalized. In this case, because the effective interaction between particles along the chain is highly nonlinear, propagation of a (dislocation-like) excitation can occur.

Transition metal oxides, and related materials, exhibit complex interplays of spin, charge, orbital, and lattice so that a simplified model such as the above should not be over-interpreted. Nevertheless, some implications are suggestive. Namely, charge-ordered states may persist up to very high temperatures, but signatures of disordered filamentary states occur at much lower temperatures with a transition to a checkerboard state at intermediate temperatures. The co-existing short- and long-range interactions will appear only upon (polaronic) localization of holes, which onsets below a characteristic temperature. Above this temperature, a more metallic-like electronic state is expected. External fields could easily induce currents along the filamentary paths in the soft phase. The soft phase at $T_s < T < T_m$ also shows similarities with the inhomogeneous states observed in manganite oxides between the true critical temperature and a higher temperature at which short-range order first appears (46). Also, some stripe-based theories for superconductivity require fluctuating stripes (47). An important feature of the soft phase is that the fluctuations are predominantly on percolating filaments rather than meandering of the filaments themselves. The fluctuating checkerboard state may thus provide a good starting point for introducing detailed local quantum-mechanical effects.

Although we have focused on a simple specific model in Eq. 4, extensive further studies have found qualitatively similar soft phase for other models with competing long- and short-range interactions. [See Ref. (33) for a comprehensive review.]

6. SUMMARY

This article is intended to illustrate the prevalence and importance of competitions and constraints as sources of mesoscopic complexity, which is so important as the bridge from microscopic to macroscopic scales in many classes of hard, soft, and biological matter (2, 3). We have emphasized the role of elasticity in strongly-correlated (quantum) materials, including many perovskites, as well as f-electron materials. Understanding the mesoscale is critical to controlling landscapes (48) of multiscale structures and to materials design with desired functionality. The examples we used are not exhaustive. For instance, competing timescales and time-dependent driving of nonlinear systems is another rich source of mesoscopic spatio-temporal patterns resulting from induced competing length scales: for instance, Ref. (49) analyzes patterns of “intrinsic localized modes,” having applications to a number of materials and condensed matter systems.

The examples we have discussed illustrate the importance of the scientific method to guide studies of materials synthesis–structure–property relationships — iterating data, models, analysis, and computation to understand, control, design, and mitigate phenomena. The future for the scientific method toolbox is very bright. The experiment/observational and computational/visualization data explosion, now joined by data analysis tools (machine

learning, artificial intelligence, etc.) for merging and even co-designing these data, is an exciting frontier. The renaissance of topology (e.g., skyrmions) and geometry, for both classical and quantum materials, will also guide future exploration — e.g., better understanding relations between structural and quantum wave-function topology (including entanglement and non-adiabatic effects), and understanding characteristic smoothing of singularities by local coupling to globally weak degrees-of-freedom. Active interfaces and thin films are very promising for technology, as control of active organic, inorganic and biological matter improves — including ultrafast spectroscopic control of charge-transfer and associated lattice changes (50).. An intriguing aspect of geometry for materials science is whether macroscopic properties depending on internal interfaces are optimized (intrinsically or by engineering) with space-filling (fractal) organization of the interfaces. Certainly, advanced (including additive) manufacturing methods will allow access to properties from materials topologies and geometries beyond even nature's evolution.

Materials play fundamental roles in the health and prosperity of society. It is not accidental that the remarkable new technologies that society is recently experiencing are accelerating in the same “century of complexity” era for science — they are both largely the results of the new experimental and simulation tools. As throughout history, the new technologies are also resulting in new societal challenges in health, energy, natural resources, climate, national security, space, cyber, social media, etc., sectors, but now at a very accelerated pace. It is fortunate that this century is generating the tools and training for the STEM workforce to play its part in addressing the societal challenges and opportunities — an

exciting time for the historic cycle of science–society compacts to make a positive future history.

ACKNOWLEDGEMENTS

J. A. (Jim) Krumhansl, a gifted polymath, began my interest in materials and microstructure and many other nonlinear phenomena. I have greatly benefited from collaborations with many colleagues, including Ken Ahn, Niels Jensen, Turab Lookman, Jim Phillips, Charles and Cynthia Reichhardt, Avadh Saxena, and Subodh Shenoy.

REFERENCES

1. Department of Energy. 2015. Quadrennial Technology Review
2. Sarrao JL, Brabtree GW (eds.). 2015. Mesoscale materials, phenomena, and functionality. *Materials Research Society*, 40.
3. LeSar R, Bishop AR, Heffner R (eds.). 1987. Competing interactions and microstructure: Statics and dynamics. *Springer Proc. in Physics*, 27.
4. Marianer S, Bishop AR. 1998. Frenkel-Kontorova model with nonconvex-interparticle interactions and strain gradients. *Phys. Rev. B* 37:9893.
5. e.g., Salje EKH. 1990. *Phase Transformations in Ferroelastic and Co-elastic Solids*. Cambridge, UK: Cambridge University Press
6. Lookman T, Shenoy SR, Rasmussen KO, Saxena A, Bishop AR. 2003. Ferroelastic dynamics and strain compatibility. *Phys. Rev. B* 67:024114
7. Curnoe SH and Jacobs AE. 2001. Time evolution of tetragonal-orthorhombic ferroelastics. *Phys. Rev. B* 64:064101
8. Krumhansl JA. 1992. In *Lattice Effects in High- T_c Superconductors*. Bar-Yam T, Egami T, Mustre de León J, Bishop AR. eds. Singapore: World Scientific
9. Asamitsu A, Moritomo Y, Tomioka Y, Arima Y, and Tokura Y. 1995. A structural phase transition induced by an external magnetic field. *Nature* (London) 373:407
10. Kartha S, Krumhansl JA, Sethna JP, Wickham LK. 1995. Disorder-driven pretransitional tweed pattern in martensitic transformations. *Phys. Rev. B* 52:803

11. Rasmussen K, Lookman T, Saxena A, Albers R, Bishop AR. 2001. Three-Dimensional Elastic Compatibility: Twinning in Martensites. *Phys. Rev. Lett.* 87:5704
12. Rowlinson JS. 1991. Symmetry of the pressure tensor in a nonuniform fluid. *Phys. Rev. Lett.* 67:406
13. Landau LD, Lifshitz EM. 1980. *Statistical Physics*. Oxford: Pergamon Press
14. Planes A, Lloveras P, Castán T, Saxena A, Porta M. 2012. Ginzburg–Landau modeling of precursor nanoscale textures in ferroelastic materials. *Continuum Mechanics and Thermodynamics* 24:619–627
15. Ahn K, Lookman T, Saxena A, Bishop AR. 2005. Electronic properties of structural twin and antiphase boundaries in materials with strong electron-lattice couplings. *Phys. Rev. B* 71:21201
16. Ahn KH, Lookman T, Bishop AR. 2004. Strain-induced metal–insulator phase coexistence in perovskite manganites. *Nature* 428:401
17. See, Mathur N, Littlewood P. 2003. Mesoscopic Texture in Manganites. *Physics Today* 56 (1):25
18. Jin S et al. 1994. Thousandfold change in resistivity in magnetoresistive La-Ca-Mn-O films. *Science* 264:413
19. Millis AJ. 1998. Lattice effects in magnetoresistive manganese perovskites. *Nature* 392:147
20. Chen, CH, Cheong SW. 1996. Commensurate to incommensurate charge ordering and its real-space images in $\text{La}_{0.5}\text{Ca}_{0.5}\text{MnO}_3$. *Phys. Rev. Lett.* 76:4042

21. Hwang HY, Cheong SW, Radaelli PG, Marezio M and Batlogg B. 1995. Lattice effects on the magnetoresistance in doped LaMnO₃. *Phys. Rev. Lett.* 75:914
22. Su WP, Schrieffer JR, Heeger AJ. 1979. Solitons in polyacetylene. *Phys. Rev. Lett.* 42:1698
23. Renner Ch, Aepli G, Kim B-G, Soh Y-A and Cheong S-W. 2002. Atomic-scale images of charge ordering in a mixed-valence manganite. *Nature* 416:518
24. Uehara M, Mori S, Chen CH and Cheong S-W. 1999. Percolative phase separation underlies colossal magnetoresistance in mixed-valent manganites. *Nature* 399:560
25. Levy P, Parisi F, Granja L, Indelicato E and Polla G. 2002. Novel dynamical effects and persistent memory in phase separated manganites. *Phys. Rev. Lett.* 89:137001
26. Lynn JW et al. 1997. Magnetic, structural, and spin dynamical properties of La_{1-x}Ca_xMnO₃. *J. Appl. Phys.* 81: 5488
27. Zhu JX et al. 2003. Elasticity-Driven Nanoscale Electronic Structure in Superconductors. *Phys. Rev. Lett.* 91:057004
28. Phillips JC, Saxena A, Bishop AR. 2003. Pseudogaps, dopants, and strong disorder in cuprate high-temperature superconductors. *Rep. Prog. Phys.* 66:2111
29. Chen A, Su Q, Han H, Enriquez E, Jia Q. 2019. Metal oxide nanocomposites: a perspective from strain, defect, and interface. *Adv. Mater.* 31:1803241
30. Gottschall T, et al. 2017. A matter of size and stress: Understanding the first-order transition in materials for solid-state refrigeration. *Adv. Funct. Mater.* 27:1606735

31. Maniadis P, Lookman T, Bishop AR. 2008. Elasticity driven self-organization of polarons. *Phys. Rev. B*. 78:134304
32. Maniadis P, Lookman T, Bishop AR. 2011. Elasticity-driven polaron patterns: Stripes and glass phases. *Phys. Rev. B*, 84:024304
33. Reichhardt C, Olson Reichhardt CJ. 2017. Depinning and nonequilibrium dynamic phases of particle assemblies driven over random and ordered substrates: A review. *Rep. Prog. Phys.* 80:026501
34. Grønbech-Jenson N, Bishop AR, Falo F, Lomdahl PS. 1992. Langevin-dynamics simulation of relaxation in large frustrated Josephson-junction arrays. *Phys. Rev. B*. 45:10139
35. Binder K and Young AP. 1986. Spin glasses: Experimental facts, theoretical concepts, and open questions. *Rev. Mod. Phys.* 58:801; Bruinsma R and Aeppli G. 1984. Interface motion and nonequilibrium properties of the random-field ising-model. *Phys. Rev. Lett.* 52:1547; Fisher DS. 1985. Sliding charge-density waves as a dynamic critical phenomenon. *Phys. Rev. B* 31:1396
36. Grønbech-Jensen N, Dominquez D, Bishop AR. 1996. Simulations of current driven three-dimensional Josephson junction arrays. *Physica B* 222:396
37. Müller KA, Takashige M, and Bednorz JG. 1987. Flux trapping and superconductive glass state in $\text{La}_2\text{CuO}_{4-y}\cdot\text{Ba}$. *Phys. Rev. Lett.* 58:1143
38. Morgenstern I, Müller KA, and Bednorz JG. 1987. Numerical simulations of a high- T_c -superconductive glass model. *Z. Phys. B* 69:33; *ibid.* 1989. 76:259
39. Lifshitz M and Slyozov VV. 1961. The kinetics of precipitation from supersaturated solid solutions. *J. Phys. Chem. Solids* 19:35; Palmer RG. 1987. In

Heidelberg Colloquium on Glassy Dynamics. van Hemmen JL and Morgenstern I, eds., *Lecture Notes in Physics* Vol. 275. Berlin: Springer-Verlag

40. Dominguez D, Grønbech-Jenson N, Bishop AR. 1995. Resistive hysteresis and nonlinear IV characteristics at the first order melting of the Abrikosov vortex lattice. *Phys. Rev. Lett.* 75:4670; and Dominguez D, Grønbech-Jenson N, Bishop AR. 1996. Metastable filamentary vortex flow in thin film superconductors. *Phys. Rev. Lett.* 76:2985
41. Olson Reichhardt CJ, Reichhardt C, Bishop AR. 2004. Fibrillar templates and soft phases in systems with short-range dipolar and long-range interactions. *Phys. Rev. Lett.* 92:016801
42. Phillips JC. 2002. Universal Intermediate Phases of Dilute Electronic and Molecular Glasses. *Phys. Rev. Lett.* 88:216401
43. Chbeir M, Bauchy M, Micoulaut M, Boolchand P. 2019. Evidence for a correlation of melt fragility index with topological phases of multicomponent glasses. *Front. Mater.* 6:1
44. Stojkovic B, et al. 2000. Electronic structure: Wide-band, narrow-band, and strongly correlated systems-Charge ordering and long-range interactions in layered transition metal oxides: A quasiclassical continuum. *Phys. Rev. B* 62:4353
45. Seul M and D. Andelman D. 1995. Domain Shapes and Patterns: The Phenomenology of Modulated Phases. *Science* 267:476
46. Burgy J, Mayr M, Martin-Mayor V, Moreo A, and Dagotto E. 2001. Colossal effects in transition metal oxides caused by intrinsic inhomogeneities. *Phys. Rev. Lett.* 87:277202

47. Carlson EW, Emery VJ, Kivelson SA, and Orgad D. 2002. Concepts in High Temperature Superconductivity. arXiv:cond-mat/0206217
48. Frauenfelder H, Bishop AR, Garcia A, Perelson A, Schusser P, Sherrington D, Swart PJ (eds.). 1997. *Landscape Paradigms in Physics and Biology*. Amsterdam: North-Holland
49. Vanossi A, Rasmussen KO, Bishop AR, Malomed BA, Bortolani V. 2000. Spontaneous pattern formation in driven nonlinear lattices. *Phys. Rev. E* 62:7353
50. Porer M, et al. 2019. Ultrafast transient increase of oxygen octahedral rotations in a perovskite. *Phys Rev Lett* 1:012005

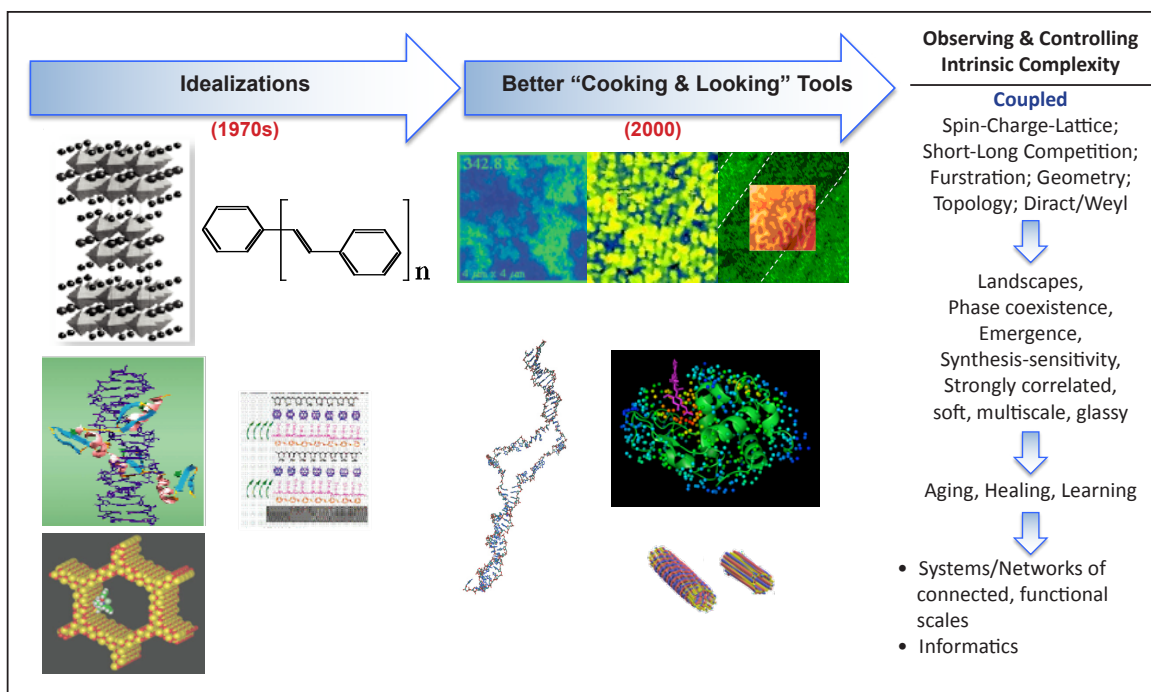


Fig. 1. Examples of an evolution of conceptual frameworks for hard, soft, and biological matter — landscapes and functional complexity. Examples shown are perovskites, DNA, molecular sieves, multilayers, and carbon nanotubes.

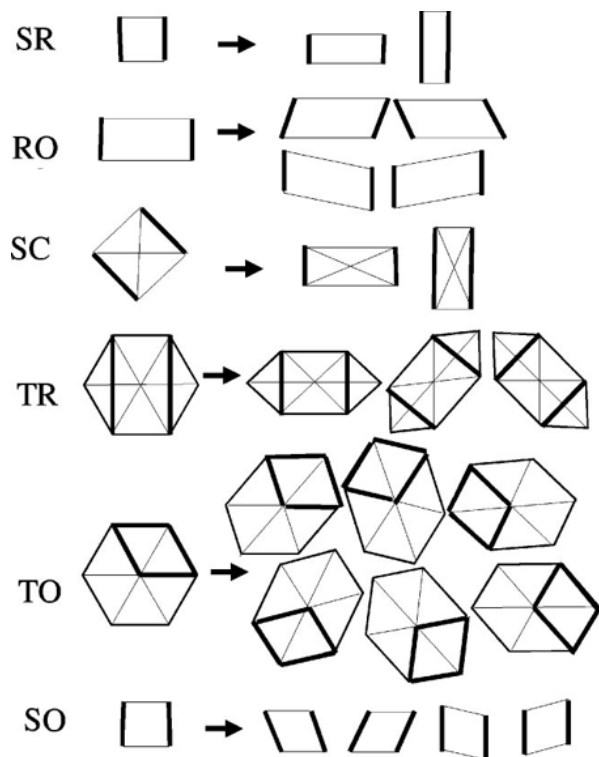


Fig. 2. Symmetry-allowed transitions in 2-d for the four crystal systems. The dark lines are guides to the eye for deformations. There is a one-component strain order parameter for (a) the SR square (S) to rectangle (R) case, driven by ε_2 ; (b) the RO rectangle to oblique (O) case, driven by ε_2 ; and (c) the SC square to centered rectangle (C) case, driven by ε_3 . A two-component OP, or two one-component OPs, lead(s) to (d) the TR triangular (T) to centered rectangle case, driven by $\varepsilon_2, \varepsilon_3$; (e) the TO triangle to oblique case, driven by $\varepsilon_2, \varepsilon_3$; and (f) the SO square to oblique case, driven by ε_2 and ε_3 , independently. Copyright 2019, American Physical Society, July 25, 2019, License number RNP/19/JUL/017073.

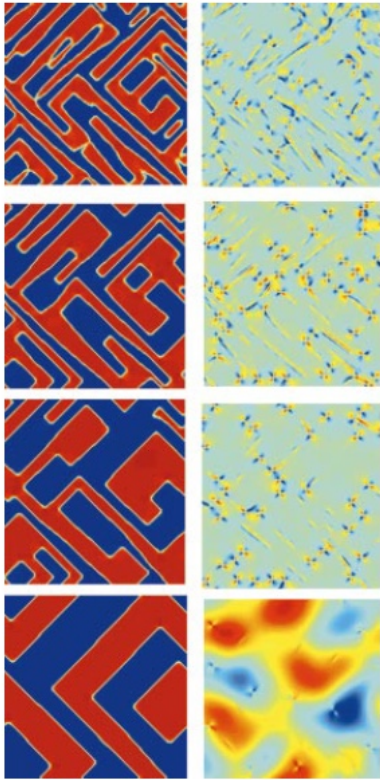


Fig. 3. Square to rectangle (SR) case: simulated interface propagation. The columns show (top to bottom) temporal sequences for time t of 40, 80, 160, and 1000 ps. The initial conditions are $\varepsilon_2(\vec{r}, t = 0), e_3(\vec{r}, t = 0)$ random around zero mean. (Parameters defined in Ref. 6.) The time step is $\Delta t = 0.002$. Left column: the OP deviatoric strain $\varepsilon_2(\vec{r}, t)$, showing domain walls propagating under the repulsive long-range compatibility potential. Right column: non-OP shear strain, $e_3(\vec{r}, t)$, propagating outwards with interfaces, concentrated at corners. Copyright 2019, American Physical Society, July 25, 2019, License number RNP/19/JUL/017073.

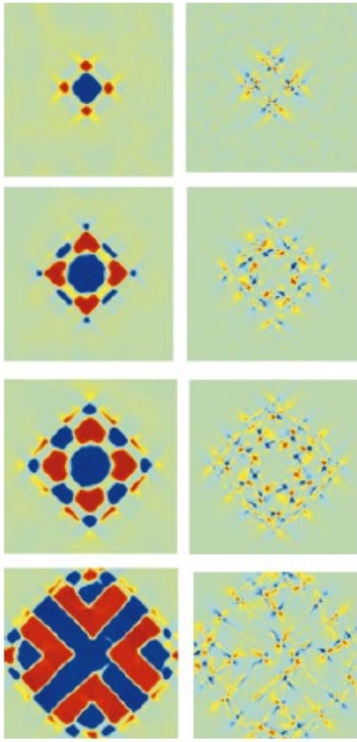


Fig. 4. SR case: simulated strain evolution, with an added fixed, time-independent, Lorentzian-profile local stress. The sequence (top to bottom), for time $t=40, 60, 76$, and 106 ps with the same parameters as Fig. 3. Left column: dynamic texturing of deviatoric strain $\varepsilon_2(\vec{r}, t)$. The system reduces the energy from the imposed single-sign strain by elastic “photo-copying,” or adaptive screening of the long-range elastic interaction, generating higher multipoles. Right column: the non-OP shear strain $e_3(\vec{r}, t)$, follows the OP propagation. Copyright 2019, American Physical Society, July 25, 2019, License number RNP/19/JUL/017073.

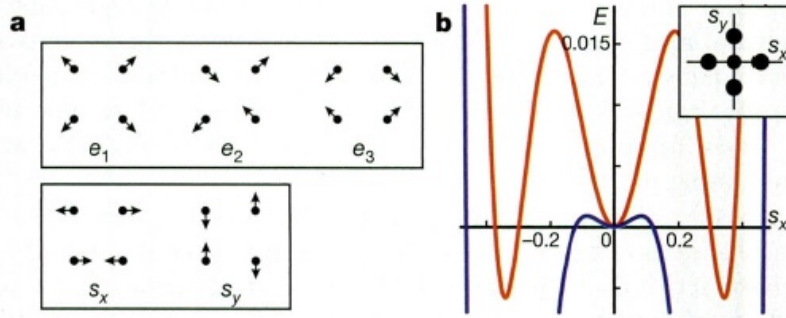


Fig. 5. Modes and energy landscape. (a) Atomic-scale lattice distortion modes (positive) for a monatomic square lattice in 2-d. (b) Energy landscape along $s_y = 0$ in $s_x - s_y$ plane for two different positive values of the harmonic modulus for short-wavelength distortion B in the energy expression below. The global minimum of the blue curve is at $E = -0.11$. The solid circles in the inset schematically represent the locations of the local minima in the $s_x - s_y$ plane. We consider the situation in which the undistorted state itself is a local energy minimum and the distorted state is the global energy minimum. The energy expression for our 2-d square lattice model is $E = E_{\text{long}} + E_{\text{short}} + E_{\text{coupling}}$, where $E_{\text{long}} = \sum_{\text{sites}} A_1 e_1^2/2 + A_2 e_2^2/2 + A_3 e_3^2/2$, and $E_{\text{short}} = \sum_{\text{sites}} B (s_x^2 + s_y^2)/2 + G_1 (s_x^4 + s_y^4)/4 + G_2 s_x^2 s_y^2/2 + H_1 (s_x^6 + s_y^6)/6 + H_2 s_x^2 s_y^2 (s_x^2 + s_y^2)/6$, and $E_{\text{coupling}} = \sum_{\text{sites}} C_3 (s_x^2 - s_y^2)/e_3$. E_{long} contains the harmonic energy for dilatation (e_1), shear (e_2) and deviatoric (e_3) long-wavelength modes, which lead to an anisotropic long-range interaction. The symmetry-allowed energy terms for short-wavelength modes (s_x, s_y) are considered up to sixth order to include features associated with the first-order phase transitions. E_{coupling} represents the coupling between short- and long-wavelength modes, where the positive C_3 is the strength of this coupling. In the homogeneous phase, all modes are independent and E can be minimized separately for

each mode. Such separate minimization gives $e_1 = e_2 = 0$ and $e_3 = -C_3 (s_x^2 - s_y^2)/A_3$, which renormalize the fourth-order coefficients and provide the condition to have both distorted and undistorted phases as local minimum states in the $s_x - s_y$ plane. Copyright 2019, Nature.

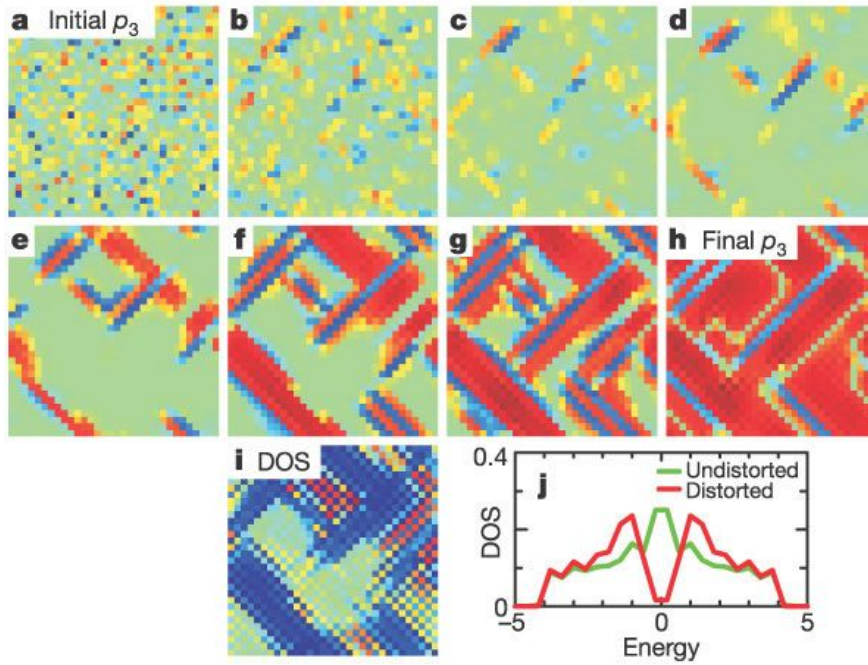


Fig. 6. Results of simulations for the shallow local minimum case (blue curve in Fig. 6b) on a 32 x 32 site lattice with periodic boundary conditions. (a) The $p_3 = s_x^2 - s_y^2$ field initial configuration. (b-g) Time-sequence of p_3 during energy relaxation. (h) Final stable stage. (Dark red and dark blue represent $\pm s_0^2$, except in (a) where they correspond to $\pm (2.6s_0)^2$. s_0 is the value of s_x or s_y at the global minimum distorted state.) (i) Local electronic density-of-states (DOS) at $\epsilon_F = 0$ for the distorted pattern in (f) (dark blue and dark red correspond to 0 and 0.5). (j) Typical local DOS versus electronic energy within the distorted and undistorted regions. The small finite DOS within the gap is due to the exponentially decaying leakage of electronic state from the metallic region: a “pseudogap.” The distorted lattice with s_x and negative e_3 , or equivalently that with s_y and positive e_3 (see Fig. 6a), leads to a gap in the DOS near electronic energy = 0. Thus if ϵ_F lies in the gap, the distorted lattice behaves as an insulator. In the structure without distortions, the DOS has no gap, and the electrons are in a

metallic state. Crucially, the study of the inhomogeneous phase shown here in (a–h) requires that lattice compatibility constraints between the distortion variables be satisfied. Elimination of e_1 , e_2 and e_3 subject to these constraint equations leads to an energy expression in terms of s_x and s_y , which is numerically minimized using various initial configurations. The electronic properties in (i) and (j) are obtained by adiabatically solving the SSH Hamiltonian on the elastic templates. Copyright 2019, Nature.

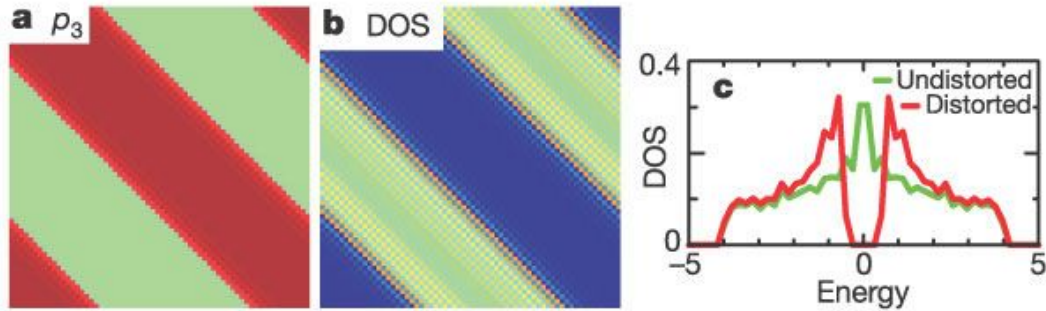


Fig. 7. Results of simulations for the deep local minimum case (red curve in Fig. 6b) on a 64 x 64 site lattice. **a.** p_3 field for the stable elastic texture (same colour scheme as Fig. 7). **b.** Local DOS configuration at $\epsilon_F = 0$. Blue and green regions are distorted insulator and undistorted metal, respectively. **c.** Typical local DOS versus energy within distorted and undistorted regions. The depth of the local energy minimum changes the nature of the inhomogeneity, from nanometre-scale fluctuations to micrometer-scale stable domains. In manganites, the harmonic modulus for the short-wavelength distortions, which changes the depth of the local energy minimum in Fig. 6b, may be varied by changing the size of the ions. The effect of the size of ions on the modulus may be represented through an additional symmetry-allowed coupling $C_1 e_1 (s_x^2 + s_y^2)$ in our model. The localized ions create an isotropic strain (e_1), which renormalizes the harmonic modulus for the short-wave-length distortion modes through this cubic anharmonic term. Other physics, such as magnetism and kinetic energy of electrons, particularly coupled with the buckling of oxygen octahedra, can also change the effective modulus and thus the energy landscape. Copyright 2019, Nature.

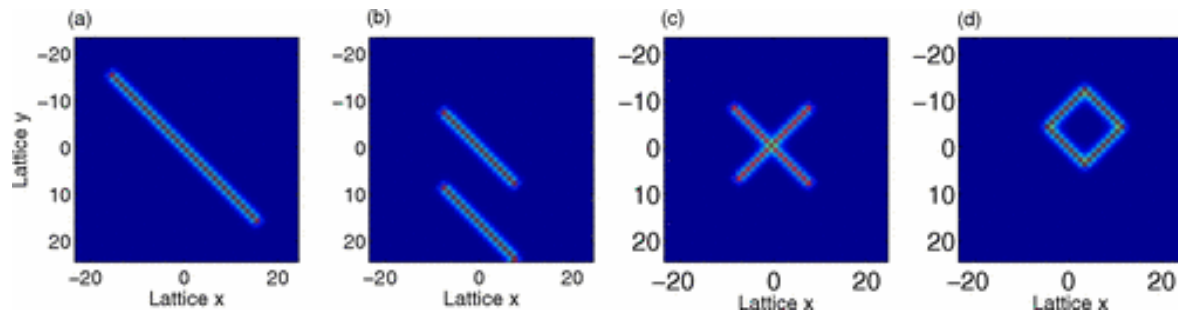


Fig. 8. (Color online) Configurations of small polarons illustrating the angular dependence of the strain field favoring diagonal strings. Copyright 2019, American Physical Society, July 25, 2019, License number RNP/19/JUL/017074.

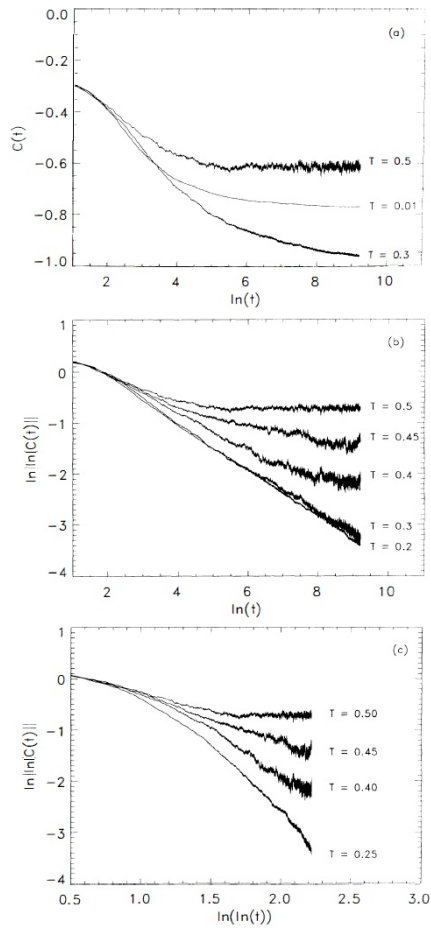


Fig. 9. Relaxation time dependence of the global correlation function $C(t)$ for frustration $f = \frac{1}{2}$ and disorder $\Delta = 0$. At $t=0$, the flux configuration is random. (a)–(c) Results for different values of the final temperature. Copyright 2019, American Physical Society, July 25, 2019, License number RNP/19/JUL/017075.

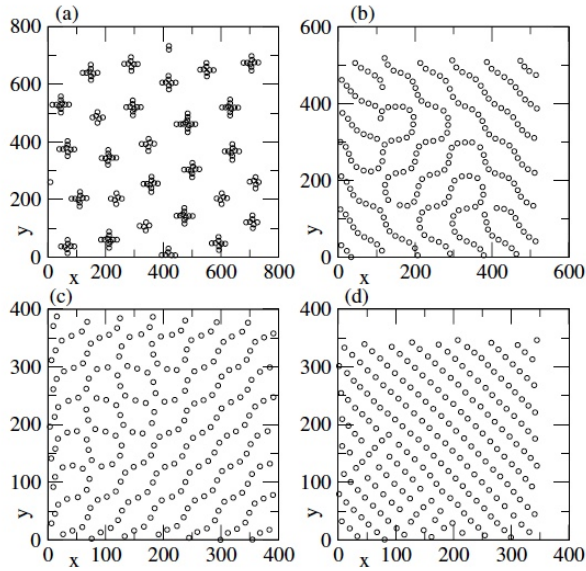


Fig. 10. Static positions of holes for different densities:(a) Clump phase, $n = 0.6$; (b) soft phase, $n = 1.2$; (c) soft phase, $n = 2.1$; (d) anisotropic Wigner crystal phase, $n = 2.7$. Copyright 2019, American Physical Society, July 25, 2019, License number RNP/19/JUL/017076.

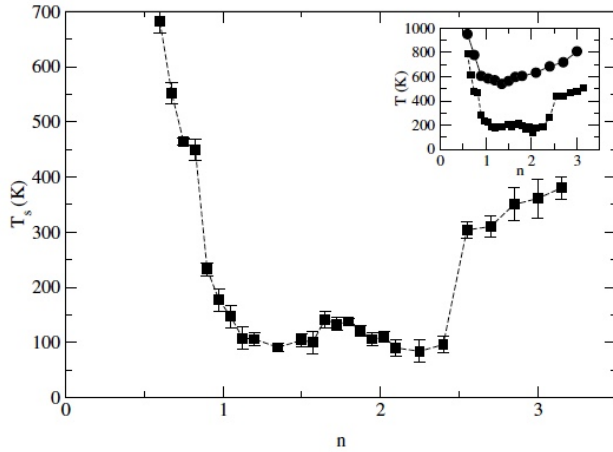


Fig. 11. Onset temperature T_s of modulated square liquid state as a function of hole density n .

Inset: Melting temperature of pattern T_m (circles) and T_s (black squares). Copyright 2019,

American Physical Society, July 25, 2019, License number RNP/19/JUL/017076.